Longwave Band-By-Band Cloud Radiative Effect and Its Application in GCM Evaluation

XIANGLEI HUANG,* JASON N. S. COLE,+ FEI HE,* GERALD L. POTTER,* LAZAROS OREOPOULOS,# DONGMIN LEE,#,@ MAX SUAREZ,# AND NORMAN G. LOEB&

* *Department of Atmospheric, Oceanic, and Space Sciences, University of Michigan, Ann Arbor, Michigan*
+ *Canadian Centre for Climate Modeling and Analysis, Environment Canada, Toronto, Ontario, Canada*
# *NASA Goddard Space Flight Center, Greenbelt, Maryland*
@ *Climate Dynamics Laboratory, Seoul National University, Seoul, South Korea*
& *Radiation and Climate Branch, NASA Langley Research Center, Hampton, Virginia*

(Manuscript received 14 February 2012, in final form 22 June 2012)

ABSTRACT

The cloud radiative effect (CRE) of each longwave (LW) absorption band of a GCM's radiation code is uniquely valuable for GCM evaluation because 1) comparing band-by-band CRE avoids the compensating biases in the broadband CRE comparison and 2) the fractional contribution of each band to the LW broadband CRE (f_{CRE}) is sensitive to cloud-top height but largely insensitive to cloud fraction, thereby presenting a diagnostic metric to separate the two macroscopic properties of clouds. Recent studies led by the first author have established methods to derive such band-by-band quantities from collocated Atmospheric Infrared Sounder (AIRS) and Clouds and the Earth's Radiant Energy System (CERES) observations. A study is presented here that compares the observed band-by-band CRE over the tropical oceans with those simulated by three different atmospheric GCMs—the GFDL Atmospheric Model version 2 (GFDL AM2), NASA Goddard Earth Observing System version 5 (GEOS-5), and the fourth-generation AGCM of the Canadian Centre for Climate Modelling and Analysis (CCCma CanAM4)—forced by observed SST. The models agree with observation on the annual-mean LW broadband CRE over the tropical oceans within ± 1 W m^{-2}. However, the differences among these three GCMs in some bands can be as large as or even larger than ± 1 W m^{-2}. Observed seasonal cycles of f_{CRE} in major bands are shown to be consistent with the seasonal cycle of cloud-top pressure for both the amplitude and the phase. However, while the three simulated seasonal cycles of f_{CRE} agree with observations on the phase, the amplitudes are underestimated. Simulated interannual anomalies from GFDL AM2 and CCCma CanAM4 are in phase with observed anomalies. The spatial distribution of f_{CRE} highlights the discrepancies between models and observation over the low-cloud regions and the compensating biases from different bands.

1. Introduction

Since the 1980s, broadband radiative flux and cloud radiative effect (CRE; the difference between all-sky and clear-sky fluxes) have been extensively used in climate studies (e.g., Ramanathan et al. 1989; Wielicki et al. 2002; Wong et al. 2006), especially in the evaluation of climate models and cloud feedback studies (e.g., Allan et al. 2004; Allan and Ringer 2003; Raval et al. 1994; Slingo et al. 1998; Wielicki et al. 2002; Yang et al. 1999). In the development of a GCM for climate studies, one inevitable and important step is "tuning," in which poorly constrained parameters are adjusted using observations and physical principles to ensure energy balance at the top of atmosphere (TOA). This ensures that simulated broadband quantities are generally consistent with the observed counterparts at the TOA. However, it cannot guarantee the consistency between band-by-band decompositions of observed and simulated radiation fluxes. In fact, quite often the compensating biases from different absorption bands offset each other and lead to a seemingly good agreement between modeled and observed broadband fluxes [e.g., see the work in the thermal infrared by Huang et al. (2006, 2007, 2008, 2010)]. Similar compensating biases can be expected in the simulated broadband CRE as well. Therefore, directly using band-by-band flux and CRE in model evaluation can avoid the compensating errors and highlight the biases in different bands since the flux and CRE of each

Corresponding author address: Prof. Xianglei Huang, Department of Atmospheric, Oceanic, and Space Sciences, University of Michigan, Ann Arbor, MI 48109-2143.
E-mail: xianglei@umich.edu

DOI: 10.1175/JCLI-D-12-00112.1

© 2013 American Meteorological Society

individual molecular absorption band are calculated directly in the GCM radiation scheme. Moreover, as illustrated in Huang et al. (2010) with both a conceptual model and numerical simulation, the fractional contribution of each band to the broadband longwave (LW) CRE (hereafter f_{CRE}) is sensitive to cloud-top height but largely insensitive to cloud fraction. The LW broadband CRE can be written as $\mathrm{CRE_{LW}} = \mathrm{fc}(F_{\mathrm{clr}} - F_{\mathrm{cld}})$ where F is the outgoing longwave flux at top of atmosphere, fc is the cloud fraction, and subscripts clr and cld denote clear sky and overcast cloudy sky, respectively. Correspondingly, the ith band CRE can be written as $\mathrm{CRE}^i = \mathrm{fc}(F^i_{\mathrm{clr}} - F^i_{\mathrm{cld}})$, and the superscript denotes the ith band. The resulting expression for f_{CRE} is

$$f_{\mathrm{CRE}} = \frac{F^i_{\mathrm{clr}} - F^i_{\mathrm{cld}}}{F_{\mathrm{clr}} - F_{\mathrm{cld}}}. \quad (1)$$

Therefore, the common factor of cloud fraction cancels and f_{CRE} is only sensitive to cloud-top temperature, making f_{CRE} a useful quantity in diagnosing and evaluating modeled CRE. The LW broadband CRE is sensitive to both the cloud fraction and (mostly) cloud-top height whereas the shortwave (SW) broadband CRE is sensitive to both the cloud fraction and (mostly) the cloud water path (i.e., cloud reflectance). Since the LW f_{CRE} is sensitive to cloud-top height but not to cloud fraction, it provides a dimension to sort out the contributions of cloud faction and cloud-top height to the broadband CRE.

Huang et al. (2008, 2010) mainly focused on the algorithm for deriving such band-by-band LW flux and CRE from the Atmospheric Infrared Sounder (AIRS) spectral radiances collocated with Clouds and the Earth's Radiant Energy System (CERES) observations from the same *Aqua* spacecraft (AIRS is a grating spectrometer; CERES consists of two broadband radiometers and one narrow-band radiometer). Using one year of data and corresponding simulations from a Geophysical Fluid Dynamics Laboratory (GFDL) AGCM (AM2), both studies also showed preliminary usage of such data in GCM evaluation. To further explore and demonstrate the potential of such band-by-band CRE in model evaluations, this study performs the first ever comprehensive evaluations of GCM-simulated band-by-band CRE from three different GCMs. The focus in this study is utilizing multiple years of data to document and compare the general features of climatology such as long-term mean, seasonal cycles, and interannual variations of CRE and f_{CRE} of each LW band. Averages over the tropical oceans will be studied and compared first in section 3. Then the spatial distributions and composite analyses with respect to large-scale circulation (represented by 500-hPa vertical velocity) will be presented in section 4.

The data and GCMs used in this study are described in section 2. Sections 3 and 4 present the comparison results. Conclusions and further discussion are given in section 5.

2. Observations and GCM simulations

a. Observations

The algorithms in Huang et al. (2008, 2010) were developed for and validated against observations over the tropical open oceans (30°S to 30°N). Hence here we employ the algorithms to derive clear-sky and all-sky spectral fluxes at a 10 cm^{-1} interval for the longwave spectrum (0–2000 cm^{-1}) using the collocated AIRS and *Aqua*-CERES observations over the tropical open oceans from 2003 to 2007. The monthly mean spectral CRE is then calculated in a similar way as the broadband CRE derived from Earth Radiation Budget Experiment (ERBE) or CERES observations. The scene type information from CERES single satellite footprint (SSF) is used with predeveloped spectral anisotropic distribution model (ADM) to invert spectral flux for each AIRS channel, and a multilinear regression scheme is then used to estimate the spectral flux over spectral regions not covered by the AIRS channels. As shown in Huang et al. (2008, 2010), the outgoing longwave radiation (OLR) derived by this approach agrees well with the collocated CERES OLR and this good agreement is found over different cloud scene types (as distinguished by distinct cloud fractions and cloud-surface temperature contrasts). Comparisons with synthetic data showed that the algorithm can reliably estimate spectral flux at 10 cm^{-1} resolution with maximum fractional difference less than $\pm 5\%$ for clear-sky scenes and $\sim\pm 3.6\%$ for cloudy-sky scenes. Details of the algorithm and validation can be found in Huang et al. (2008, 2010).

Table 1 summarizes the comparison between OLR derived by this spectral ADM approach with the collocated CERES OLR for 2003 to 2007. AIRS version 5 calibrated radiances and CERES SSF edition 2 data are used. The 2σ radiometric calibration uncertainty of CERES OLR is $\sim 1\%$, which translates to ~ 2.5 W m^{-2} for a typical OLR value in the tropics. Table 1 shows that, for all the years, the mean difference between CERES clear-sky OLR and our derived clear-sky OLR is always below the 2σ uncertainty. The cloudy-sky OLR mean difference is about the same as the 2σ uncertainty. The standard deviations of these differences change little from year to year.

b. GCMs

We used three atmospheric general circulation models in this study, the GFDL AM2 model (Anderson et al.

TABLE 1. Difference between OLR estimated from AIRS spectra with algorithms described in Huang et al. (2008, 2010), denoted as OLR_{AIRS_huang}, and OLR from collocated CERES measurements, denoted as OLR_{CERES}. Only observations over the tropical oceans are used here. Number of collocated observations as well as the mean difference and standard deviation are listed for each year as mean ± standard deviation.

	Clear sky over the ocean		Cloudy sky over the ocean	
	Number of observations	$OLR_{AIRS_huang} - OLR_{CERES}$ (W m^{-2})	Number of observations	$OLR_{AIRS_huang} - OLR_{CERES}$ (W m^{-2})
2003	1.05×10^6	0.84 ± 1.56	1.18×10^7	2.66 ±5.68
2004	1.08×10^6	0.67 ±1.52	1.24×10^7	2.15 ±5.51
2005	1.08×10^6	1.42 ±1.68	1.26×10^7	2.88 ±5.79
2006	1.08×10^6	1.55 ±1.74	1.27×10^7	2.94 ±5.92
2007	1.04×10^6	1.73 ±1.86	1.27×10^7	3.00 ±5.92

2004), the Fortuna 2.2 version of the National Aeronautics and Space Administration (NASA) Goddard Earth Observing System version 5 (GEOS-5; Molod et al. 2012), and the fourth-generation AGCM at the Canadian Centre for Climate Modelling and Analysis (CCCma), Environment Canada (CanAM4; von Salzen et al. 2012, manuscript submitted to *Atmos.–Ocean*). Each GCM is forced with observed SSTs over multiple years. For each model, clear-sky flux and all-sky fluxes of the individual bands of the LW radiative transfer code are directly saved in the output of simulations. For GEOS-5 and CanAM4, the simulations were carried out for 2000–09, but only the 2003–07 period is analyzed and compared with observations here. For AM2, because of limited resources, the simulation was carried out only up to 2005 so only the simulations from 2003 to 2005 are analyzed here. As will be shown in the next section, the year-to-year variations of band-by-band CRE and f_{CRE} are small so the different period in the AM2 simulations has little effect on the comparisons of long-term mean and mean seasonal cycle.

The longwave radiation scheme in the GFDL AM2 model follows Schwarzkopf and Ramaswamy (1999). The LW spectrum is divided into eight bands, with two water bands (far-IR and >1400 cm^{-1}) treated together, in practice. Clouds are assumed to be nonscattering in the LW. The LW radiation scheme in the NASA GEOS-5 is based on Chou et al. (2003). It divides the LW spectrum into nine bands and can be run at two accuracy modes (the high accuracy mode is used here) using either a *k*-distribution or lookup table approach to calculate gaseous transmission functions. Cloud scattering in the LW is handled empirically using a rescaling approach. In the CanAM4 model, the optical properties of gases are modeled using a correlated-*k* distribution (Li and Barker 2005) while the radiative transfer is simulated using the Monte Carlo independent column approximation and two-stream radiative transfer solutions (von Salzen et al. 2012, manuscript submitted to *Atmos.–Ocean*; Pincus et al. 2003; Li 2002). Scattering by clouds droplets is included based on the absorption approximation (Li and Fu 2000). Note that both the GEOS-5 and CanAM4 models take into account the scattering of cloud in the longwave.

As in Huang et al. (2008, 2010), the spectral CRE derived from the AIRS data is averaged onto the 2° latitude × 2.5° longitude grid box, the same horizontal resolution of the GFDL AM2 and NASA GEOS-5 models. The horizontal resolution of CCCma CanAM4 is 2.8° × 2.8°.

c. *Redefining the bands for comparison*

Because of the different radiation schemes used in the three GCMs, the number of bands and the bandwidth for each band are not necessarily the same. In fact, GFDL AM2 uses 8 bands in the LW while NASA GEOS-5 uses 10 bands and CanAM4 uses 9 (Table 2). To facilitate the comparison, we define five new bands (Table 2) to be used for comparisons between GCMs and between GCMs and observations, each of which is either a band common to the GCM radiative transfer schemes or some combination of bands used in the GCMs. This ensures the maximum compatibility among GCMs for the band-by-band comparisons. As shown in Table 2, after merging into five bands, the bandwidth structures of GEOS-5 and CanAM4 models are for the most part consistent with each other and consistent with the five bands defined for the observational analysis. AM2 bandwidths are slightly different. To understand the effect of such intrinsic differences in the bandwidths in the GCMs on the band-by-band fluxes and CREs, we compute the flux of each band (F_{model_bnd}) for a blackbody at a temperature T using the bandwidth from each GCM. This flux is then compared to the flux of the band defined for this study (F_{bnd}). The relative difference, $(F_{model_bnd} - F_{bnd})/F_{bnd}$, is shown in Fig. 1 for $T = 220$ K and $T = 298$ K, respectively. Except for band 4 (ozone band, 980–1100cm^{-1}) and band 5 (1100–1400 cm^{-1}), the relative difference due to the varying bandwidths is within 10% (Figs. 1a,b). By subtracting the flux for $T = 298$ K from the flux for $T = 220$ K,

TABLE 2. The LW bands used in each GCM as well as the five bands used in this study for the comparisons across all GCMs and observations. The bandwidths are given in wavenumber (cm^{-1}). The major absorbers of each band are also listed.

Major absorber(s)	Band used in this study (cm^{-1})	GFDL band ID	GEOS-5 band ID	CanAM4 band ID
H_2O	Band 1: 0–560 and >1400	Bands 1 and 8 (0–560 and >1400)	Bands 1 and 2 (0–540) and bands 8 and 9 (>1380)	Bands 1–3 (>1400) Bands 8 and 9 (0–540)
CO_2	Band 2: 560–800	Band 2 (560–800)	Bands 3 and 10 (540–800)	Band 7 (540–800)
H_2O continuum	Band 3: 800–980	Band 3 and 4 (800–990)	Band 4 (800–980)	Band 6 (800–980)
O_3	Band 4: 980–1100	Band 5 (990–1070)	Band 5 (980–1100)	Band 5 (980–1100)
H_2O continuum; CH_4, N_2O	Band 5: 1100–1400	Band 6 (1070–1200) Band 7 (1200–1400)	Band 6 (1100–1215) Band 7 (1215–1380)	Band 4 (1100–1400)

which mimics the magnitude of LW CRE (Fig. 1c), we find that the relative difference for each band in each GCM's radiation scheme is about the same. The largest relative difference is ~33% and always occurs in the ozone band. This larger error occurs because of the rapid decrease of the blackbody curve between 220 and 298 K over this band, which causes the small bandwidth differences between AM2 and GEOS5–CanAM4 to lead to large fractional difference in flux. For this reason, we omit here the ozone band (band 4) in some analyses presented in sections 3 and 4. If an ozone band result is discussed, it must be interpreted with caution for the GFDL AM2, which has a different bandwidth for the band from the other two GCMs and the observations. For most of the analysis, our focus is primarily on bands 1, 2, and 3, for which the intrinsic bandwidth differences in the GCMs yield no more than 10% relative difference in the flux, CRE, and f_{CRE}.

3. Model intercomparisons and comparisons with observations: Averages over the tropical ocean

Figure 2 shows the 5-yr averages of all-sky OLR and LW CRE from the NASA GEOS-5 and CCCma CanAM4 model simulations, 3-yr averages from the GFDL AM2 simulation, and the counterpart 5-yr averages from the collocated AIRS and CERES observations (hereafter, referred to as "observations" for brevity). Generally the models and the observations are consistent with each other on the broad spatial features of both all-sky OLR

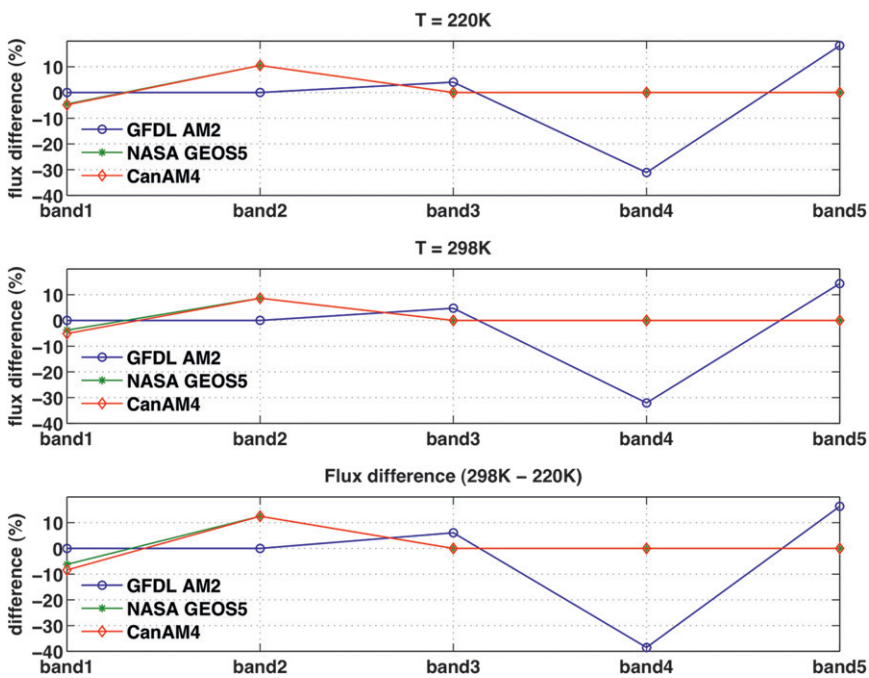

FIG. 1. (a) The percentage flux difference due to differences between intrinsic GCM bandwidths defined in each GCM and the bandwidths used in this study (refer to Table 2 for the details). Flux is calculated for a blackbody at 220 K. (b) As in (a), but for a blackbody at 298 K. (c) The flux difference between (a) and (b) expressed in percentage.

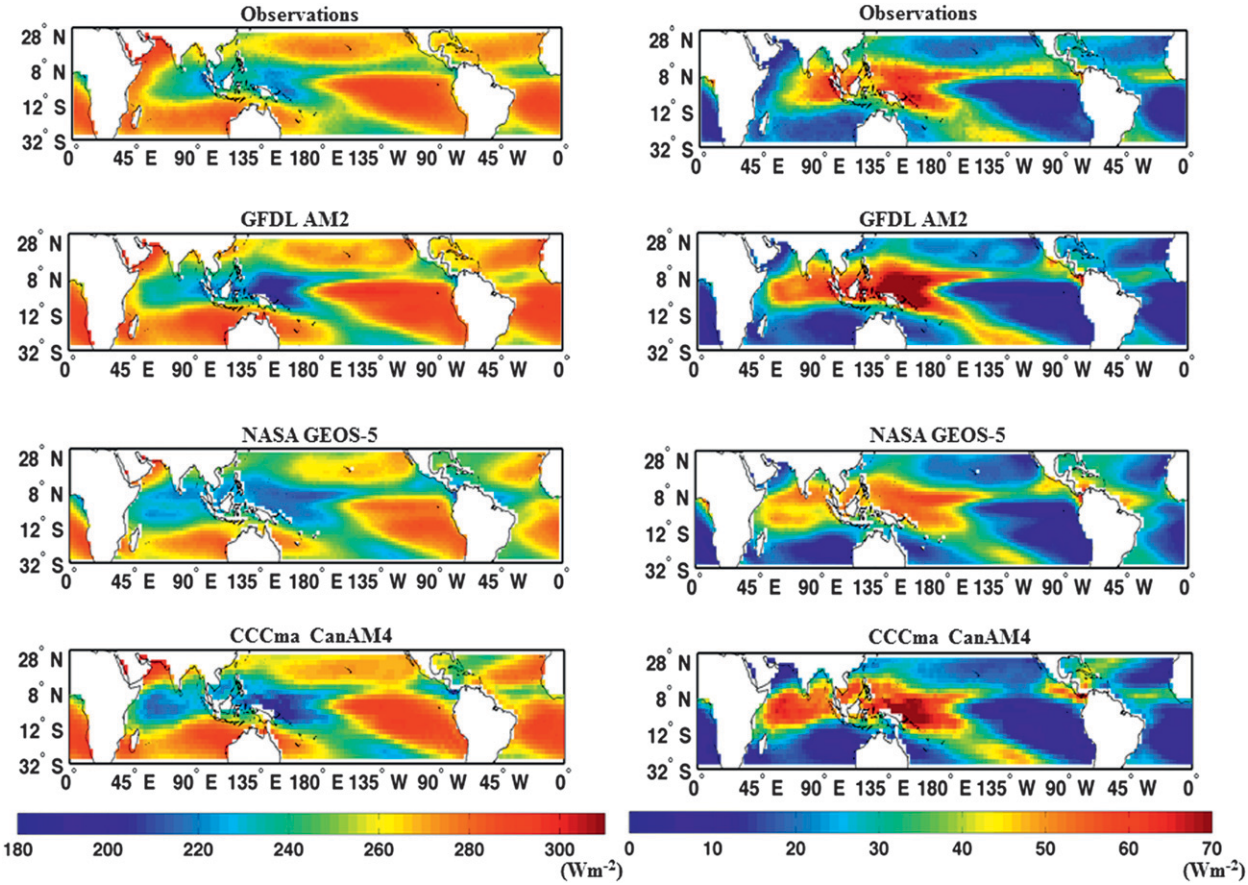

FIG. 2. The multiyear mean of (left) all-sky OLR and (right) LW broadband LW CRE derived from collocated (top to bottom) AIRS and CERES observations and the GFDL AM2, NASA GEOS5, and CCCma CanAM4 model simulations. Note that color scales are different for the left and right panels.

and longwave CRE. In the tropical Pacific warm pool east of the Maritime Continent, the AM2 and CanAM4 models have lower all-sky OLR than the observation and the GEOS-5 model. Accordingly, their LW CREs are higher than those in the observations and the GEOS-5 model. The LW CRE is only ~10 W m^{-2} (or even smaller) over the oceans west of major continents because these regions are frequently covered by marine stratus with cloud top ~1 km and thus have little thermal contrast with surface. Judging from the LW broadband CRE here alone, observations and all GCMs seemingly agree better over the low-cloud regions than over the high-cloud regions such as the ITCZ and Southern Pacific convergence zone (SPCZ). However, as we shall show in the following subsections, the f_{CRE} over the low-cloud regions is indeed quite different among the GCMs and between the models and observations.

a. Long-term means and seasonal cycles

Table 3 summarizes the multiyear means of the LW broadband and band-by-band CREs averaged over the entire tropical oceans. Observed long-term mean LW broadband CRE is 28.5 W m^{-2} while the model results are slightly lower by 0.2–1.2 W m^{-2} (i.e., 0.7%–4% smaller). However, the absolute difference in the CRE of a particular band could be easily as large as, or even larger than, the absolute broadband difference (hence fractional difference in a band could be much larger than that in broadband). For example, the differences between observed and simulated CREs in band 2 (the CO_2 band) are ~−0.6 to 0.7 W m^{-2} (−14% to +16% difference). The difference between observed and CanAM4-simulated CRE in band 1 alone is ~1.12 W m^{-2} (~20% difference). Modeled broadband CREs are always smaller than the observed CRE, but modeled CREs in a given band could be either larger or smaller than their observed counterparts. Such compensation among bands leads to an apparent good agreement of the broadband LW CRE. Band-by-band CREs exposes such compensation in a quantitative way and makes it possible to further examine the sources of the compensating biases.

TABLE 3. Multiyear means of LW broadband and band-by-band CRE averaged over the tropical oceans. The numbers in parentheses are the fractional contribution to the total LW broadband CRE (f_{CRE}). The AM2 results for band 4 are in italics to denote the prominent bandwidth differences between the GFDL AM2 model and the other two GCMs and observations (refer to section 2 for detailed discussions).

	Observation (W m^{-2})	GFDL AM2 (W m^{-2})	NASA GEOS-5 (W m^{-2})	CCCma CanAM4 (W m^{-2})
LW broadband	28.5 (100%)	28.0(100%)	28.3 (100%)	27.3 (100%)
Band 1: 0–560 and >1400 cm^{-1}	5.59 (19.6%)	5.31 (19.0%)	5.11 (18.1%)	4.47 (16.3%)
Band 2: 560–800 cm^{-1}	4.33 (15.2%)	3.72 (13.3%)	5.07 (18.0%)	4.82 (17.6%)
Band 3: 800–980 cm^{-1}	9.25 (32.4%)	9.96 (35.6%)	9.03 (32.0%)	8.80 (32.2%)
Band 4: 980–1100 cm^{-1}	3.72 (13.0%)	*1.68 (6.0%)*	3.63 (12.9%)	3.75 (13.7%)
Band 5: 1100–1400 cm^{-1}	5.62 (19.7%)	7.32 (26.2%)	5.41 (19.2%)	5.50 (20.1%)

Among the five bands examined here, the largest contributor to LW CRE is band 3, the first window region from 800 to 980 cm^{-1}, which is responsible for ~(32–36)% of LW CRE. There is a large discrepancy in the CRE of band 4 (ozone band) between the AM2 model and the other two models and the observations. As mentioned in section 2, the AM2 model has a different bandwidth for band 4 while others have identical bandwidth. Second, the AM2 simulation here is done with prescribed climatological ozone profiles at the 1990s level obtained from a combination of ozonesonde and satellite measurements (Paul et al. 1998; Anderson et al. 2004). In contrast, the GEOS-5 model ozone fields are calculated online inside the GCM using a parameterization described in Rienecker et al. (2008). The CanAM4 simulation used a zonally averaged version of the Atmospheric Chemistry and Climate (AC&C)/Stratospheric Processes and Their Role in Climate (SPARC) ozone database that was prepared for phase 5 of the Coupled Model Intercomparison Project (CMIP5) model simulations (Cionni et al. 2011). Over the historical period, the database consists of time-varying ozone fields based on observations for the stratosphere and chemistry–climate model simulations for the troposphere. Band 4, the ozone band, never saturates, which makes it sensitive to stratospheric and tropospheric ozone as well as to surface and cloud temperatures. Moreover, ozone spatial distribution is indeed affected by the large-scale circulation and transport. Therefore, besides the bandwidth discrepancies, whether realistic online ozone fields are available or not could potentially affect the simulated CRE results as well.

Seasonal cycles of CREs of bands 1–3 are shown in Fig. 3. Compared to the mean values shown in Table 3, the seasonal fluctuation is very small (~3.5% or even smaller). For both models and observations, band CRE seasonal cycles closely track one another. The observations show two peaks with one in April–May and the other in November–December, which is related to the movement of the sun as well as to the north–south seasonal movement of ITCZ. The models also show such semiseasonal cycles with similar phase except that the first peak in the GEOS-5 is one month ahead of the observations. Although the phases are generally consistent with each other, the magnitudes of the seasonal cycles are noticeably different by about a factor of 2, with the observations and GEOS-5 having similar amplitudes and those of AM2 and CanAM4 being much smaller.

The good phase syncing between CREs of different bands is largely due to the fact that for all the LW bands the surface and cloud-top temperature contrast is the largest driver of CRE. Therefore, they all vary in phase with the LW broadband CRE in terms of the absolute magnitude. Seasonal cycle of the f_{CRE} (Fig. 4) is different because the LW broadband CRE is always normalized to 100% for each month. In contrast to the seasonal cycle of absolute band CRE (Fig. 3), for both models and observations a single annual cycle is dominant instead of a semiannual cycle. The seasonal cycle of band 1 (water vapor band) f_{CRE} is strongly anticorrelated with that of band 3 (the window region) f_{CRE}. For both models and the observation, band 1 peaks in March–April whereas band 3 peaks in July–August. This suggests that any phase discrepancies shown in Fig. 3 are likely dominated by differences in cloud fraction rather than differences in cloud-top height (otherwise, the same discrepancies would have appeared in such f_{CRE} seasonal cycles as well). For f_{CRE} seasonal cycles, the GCMs have similar amplitudes but are 2–3 times smaller than the observed amplitude (Fig. 4).

Figure 4 also shows that the seasonal cycle of band 2 f_{CRE} closely tracks that of band 1 but is anticorrelated with that of band 3. Figure 5 plots the correlation coefficients between the seasonal cycle of band 1 f_{CRE} and the seasonal cycle of f_{CRE} of the remaining bands. Models and observations behave similarly in terms of such interband correlations: window bands (bands 3 and 5) are strongly anticorrelated with band 1. The observations exhibit a moderate positive correlation between bands

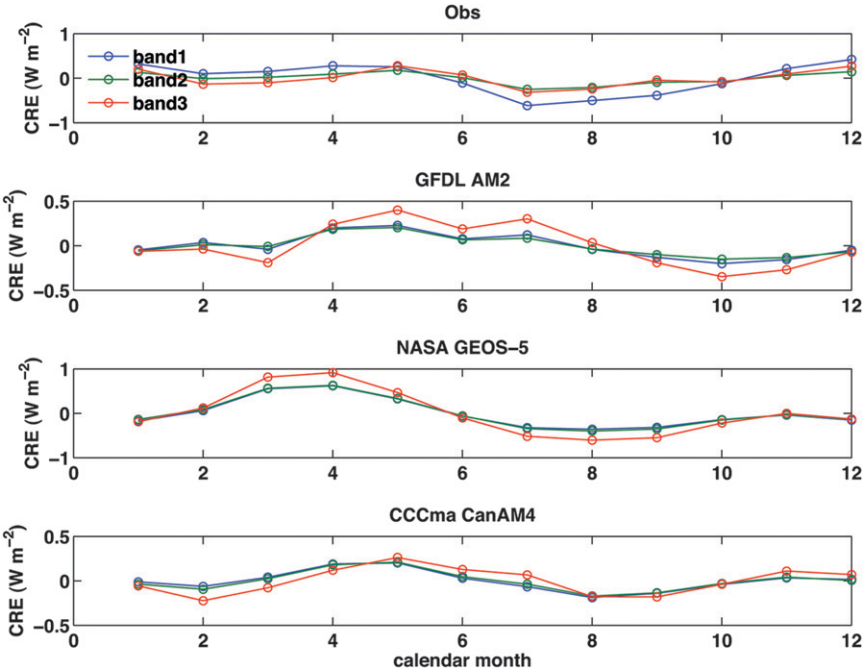

FIG. 3. The mean seasonal cycles of Band1 CRE (blue lines), Band2 CRE (green lines), and Band3 CRE (red lines). Definitions of bandwidths can be found in Table 2. For better visualization, CREs from the observation and GEOS-5 model are plotted on one scale (± 1 W m^{-2}) and those from the AM2 and CanAM4 model are plotted on another scale (± 0.5 W m^{-2}).

2 and 1 while much stronger positive correlations are seen for the GCMs. The largest discrepancies exist in band 4 (the ozone band). As expected, band 4 f_{CRE} in observations, GEOS-5, and CanAM4 shows a strong in-phase relation with band 3 f_{CRE}, since cloud and surface thermal contrast significantly affects both bands. For the AM2 model, the correlation between band 4 and band 3 f_{CRE} is weak, partly due to the prescribed climatological ozone profiles. Such differences indicate the benefit of having realistic or self-consistent ozone profiles in the transient simulations.

b. *Interpretation of the seasonal cycles*

To understand the seasonal cycles shown in Figs. 3 and 4, it is instructive to look the seasonality of cloud macroscopic properties averaged over the tropical oceans. Figure 6a shows the International Satellite Cloud Climatology Project (ISCCP; Rossow and Schiffer 1991, 1999) long-term mean seasonal cycles of cloud fractions for high, middle, and low cloud, respectively. The peaks of high-cloud fraction can be found during two periods: April–May and November–January, the latter being also the peak for middle-cloud fraction. The seasonality of high-cloud and middle-cloud fraction is consistent with the observed seasonal cycles of band-by-band CRE in Fig. 3. Meanwhile, even though the low-cloud fraction peaks in July–August, it contributes little to the observed seasonal cycle of CRE because low clouds contribute little to the absolute LW CRE or the absolute band CRE.

Figure 6b shows the ISCCP mean seasonal cycle of cloud-top pressure (CTP) averaged over the tropical oceans. In contrast to the seasonality of cloud fractions, it shows that mean cloud top is highest in April–May and lowest in August–September. As shown in Fig. 7b in Huang et al. (2010), the higher the cloud top, the larger band 1's contribution to the total LW CRE and the smaller band 3's contribution. This behavior is mainly due to the shift of blackbody peak emission toward lower frequency as the cloud-top temperature becomes colder (i.e., Wien's displacement law). Therefore, the seasonality of CTP is consistent with the observed seasonality of f_{CRE} in Fig. 4. Note that even band 1 has one subband (0–560 cm^{-1}) with frequency lower than band 3 and the other subband (>1400 cm^{-1}) with frequency higher than band 3, but the 0–560 cm^{-1} subband always dominates the flux of band 1 for the range of temperatures of our interest. The H_2O ν_2 band (>1400 cm^{-1}) is at the far tail of the branch of blackbody emission curve where radiance is nearly exponentially decay with the frequency. As a result, its contribution to the flux is always small. For example, for a blackbody at 288 K, 84.8% of band 1 flux originates from the 0–560 cm^{-1} subband; for a blackbody at 210 K, 97.8% of band 1 flux is from the

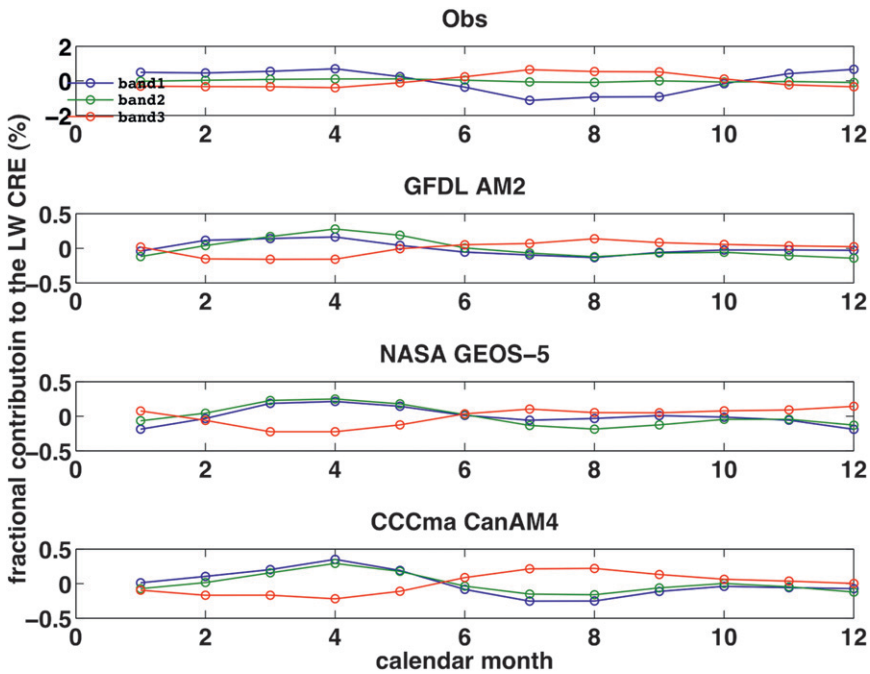

FIG. 4. The mean seasonal cycle of f_{CRE}, the fractional contribution of a band to the total LW CRE. Bands 1–3 are plotted in blue lines, green lines, and red lines, respectively. (top to bottom) AIRS and CERES observations and the GFDL AM2, NASA GEOS5, and CCCma CanAM4 model simulations.

0–560 cm^{-1} subband. This is why we can still use Wien's displacement law to explain the relative importance of the contributions of bands 1 and 3.

Given the strong anticorrelation between band 1 f_{CRE} and band 3 f_{CRE}, it is worthwhile to explore to what extent we can use the ISCCP mean seasonal cycle of CTP to estimate the amplitudes of the seasonal cycles of bands 1 and 3. For both seasonal cycles, we use the standard deviation as a measure of the amplitude. Similar to Huang et al. (2010), we assume a layer of optically thick cloud ($\tau \gg 1$) and typical tropical sounding profiles of temperature, humidity, and ozone (McClatchey et al. 1972). Then we vary the cloud top from the lower troposphere to the upper troposphere and use MODTRAN5 (Berk et al. 2005) to calculate the f_{CRE} of bands 1 and 3 accordingly (Fig. 7a). When the cloud top is lower than 600 hPa, band 1 f_{CRE} is less than ~6% whereas band 3 f_{CRE} is more than 40%. As the cloud top moves upward, the contribution from band 1 gradually increases while that from band 3 decreases. When the cloud top reaches 150 hPa, the contributions from both bands are essentially equal ($f_{CRE} \sim 28\%$). Figure 7a also shows that, above 600 hPa, the change of the fractional contribution with respect to cloud-top pressure is nearly linear. Therefore, we define the linear regression slope for the ith band as

$$r_i = \frac{df^i_{CRE}}{d\mathrm{CTP}}, \tag{2}$$

where superscript i denotes the ith band; r_1 and r_3 are then derived by linear regression of the curve shown in Fig. 7a. Then the amplitude of seasonal cycle of band 1 (band 3) can then be estimated by multiplying r_1 (r_3) by the standard deviation of ISCCP CTP seasonal cycle in Fig. 6b, which is 12.2 hPa. Figure 7b shows the amplitudes estimated in this manner versus the real amplitudes derived from Fig. 4, top panel. The simple estimations are 82% and 85% of the observed values for bands 1 and 3, respectively. No cloud fraction values are involved in this estimation, which corroborates the fact that the fractional contribution of each band is largely insensitive to cloud fraction but is mainly affected by changes in cloud-top pressure. This behavior is very different from that of the absolute amount of band-by-band CRE, which is largely influenced by the fractions of high cloud and middle clouds.

Since the ISCCP CTP seasonality can largely explain the observed seasonality of f_{CRE}, the model–observation discrepancies shown in Fig. 4 should be largely due to the difference in observed and simulated seasonal cycles of CTP, especially the amplitudes. Using the same slopes of r_1 and r_3 derived above, we estimate that the

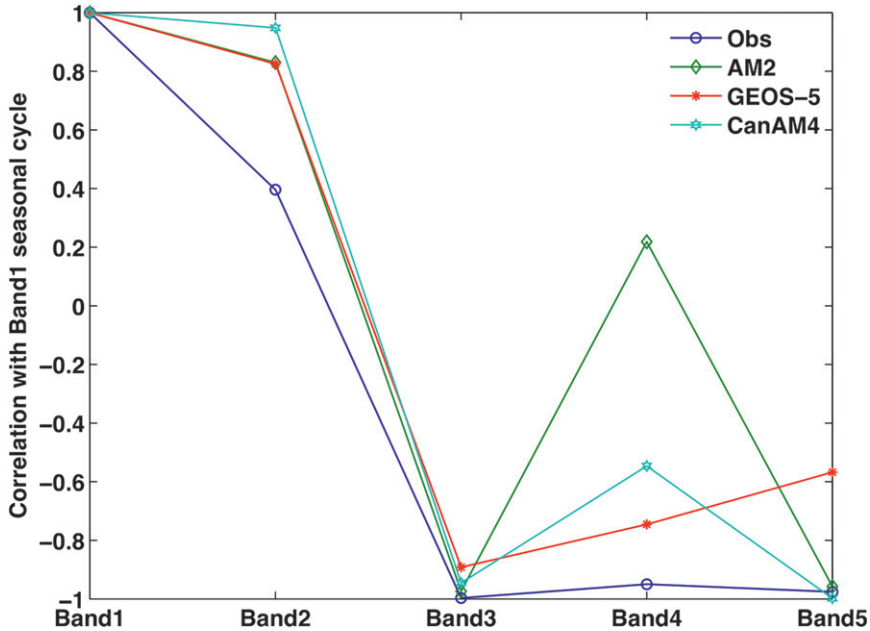

FIG. 5. Correlation coefficients between the mean seasonal cycle of band 1 and that of all other bands. The observed relation is plotted in blue. The GFDM AM2, NASA GEOS-5, and CanAM4 models are plotted in green, red, and cyan lines, respectively.

amplitudes (the standard deviations) of CTP seasonal cycles for AM2, GEOS-5, and CanAM4 models are 2.9, 3.7, and 4.7 hPa, respectively (in comparison to the 12.2 hPa derived from ISCCP's mean CTP seasonal cycle).

c. *Interannual variations*

Figure 8 shows the 5-month running means of deseasonalized time series of CRE along with the ENSO index. Following several previous studies (Deser and Wallace 1990; Fu et al. 1996; Klein et al. 1999), the ENSO index is defined as the 5-month running mean of deseasonalized SST anomalies averaged over the tropical eastern Pacific (defined as the area between 5°S and 5°N and the South American coast and 180°W). The amplitude of interannual variation of LW broadband CRE is ~0.5 W m^{-2}. The running-mean time series of observed CRE and those of simulated by the AM2 and CanAM4 models are positively correlated with the ENSO index. They tend to have positive anomalies when the eastern Pacific SST anomalies are also positive (i.e., the El Niño state). GEOS-5 (red line in Fig. 8a) shows a different response to the ENSO index. The correlation between GEOS-5 broadband LW CRE time series and the ENSO index is slightly positive (~0.02) but not statistically significant. The variation of each band CRE anomalies with the ENSO index closely follows the variation of LW broadband CRE anomalies, as shown in Fig. 8b for band 1 (results from other bands not shown here).

When the 5-month running mean of the deseasonalized anomalies of f_{CRE} is correlated with the ENSO index (Fig. 9), all three models agree with the observation on the signs of correlations over all bands except band 4 (the ozone band). The correlation with the ENSO index is positive for band 1 (the H_2O band) and negative for bands 3 and 5 (the window bands). Correlations using the observations tend to be smaller than those from the simulations, which reflects either the noisy nature of the observations or the model deficiencies that lead to overly strong correlations between f_{CRE} and ENSO index, or both. The correlations in Fig. 9 indicate to a large extent how the cloud-top height varies at the interannual time scale with the ENSO index. Both the observation and models suggest that, averaged over the entire tropical ocean, the mean infrared effective cloud top averaged over the tropical oceans tends to be elevated when the ENSO index is positive (El Niño state) and vice versa.

4. Model intercomparisons and comparisons with observations: Spatial distributions and composite analysis

a. *Spatial distributions*

Discussions in the previous section were about the averages over the entire tropical oceans. In this section, spatial distributions of band-by-band CRE and f_{CRE} are to be discussed. As explained in section 1, the map of

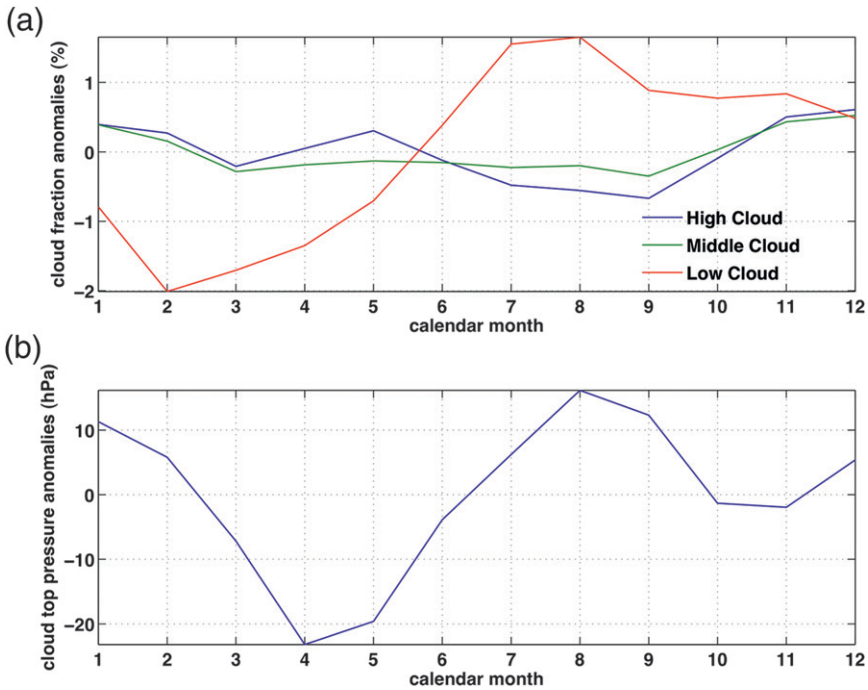

FIG. 6. (a) The ISCCP climatological seasonal cycle (deviations from the climatological mean) of cloud fraction for high cloud (blue), middle cloud (green), and low cloud (red) averaged over the tropical oceans. (b) The ISCCP climatological seasonal cycle of cloud-top pressure averaged over the tropical oceans.

absolute CRE of a particular band largely resembles the map of broadband LW CRE (right panels in Fig. 2) and highlights the contrast of absolute CRE between regions featuring high clouds [where broadband LW CRE is ~(60–80) W m^{-2}] and regions dominated by low clouds [where broadband LW CRE is ~(10–20) W m^{-2} or even less]. Therefore, in this section the focus is on the spatial distributions of f_{CRE}. Because the broadband and band-by-band CRE provide similar information, we mainly focus on the spatial distributions of f_{CRE} in this section.

Figure 10a shows the observed band 1 f_{CRE}. As expected, the largest values of f_{CRE} [~(0.25–0.35)] are found over the regions with frequent occurrence of high clouds, such as ITCZ, SPCZ, and Indian monsoon regions. The smallest values occur in regions frequently covered by marine stratus (i.e., low cloud), such as the Pacific coast off South America, the Namibia coast, and the ocean region west of Australia. Figures 10b–d show the differences between modeled and observed band 1 f_{CRE}. Simulated climatological mean positions of ITCZ over the equatorial Pacific and Atlantic are south of the observed ones, and the widths of ITCZ are also different, which accounts for the negative differences north of 8°N and the slight positive differences between 0° and 8°N of the tropical Pacific and Atlantic. For regions where low clouds are prevalent, modeled f_{CRE} values are usually higher than the observed ones but the three models largely agree with each other.

For band 2 (CO_2 band; Fig. 10e), the contrast in f_{CRE} between high-cloud and low-cloud regions (0.16 vs 0.11) is much smaller than that of band 1 (0.3 vs 0.05). The models largely disagree with each other (Figs. 10f–h) on the spatial distribution of f_{CRE}. Compared to the observation, AM2 considerably underestimates band 2 f_{CRE} over the low-cloud regions but largely agrees with observations over the rest of tropical oceans. GEOS-5 uniformly overestimates band 2 f_{CRE} everywhere over the tropical oceans by ~(0.02–0.04) with slightly larger overestimates for parts of the low-cloud regions. CanAM4 exceeds observations by ~(0.02–0.04) for the tropical oceans except the low-cloud region, where the difference is indeed slightly negative, between −0.02 and 0.

The observed band 3 f_{CRE} (Fig. 11a) peaks over the low-cloud regions and drops over the high-cloud regions. This is consistent with the variation of band 3 f_{CRE} with cloud-top pressure (e.g., Fig. 7a). Compared to the observation, the AM2 model overestimates band 3 f_{CRE} nearly uniformly over the entire tropical oceans by ~0.04. The GEOS5 and CanAM4, on the other hand, underestimate band 3 f_{CRE} over the low-cloud regions and are close to the observations for the rest regions of the domain with only slight positive or negative differences.

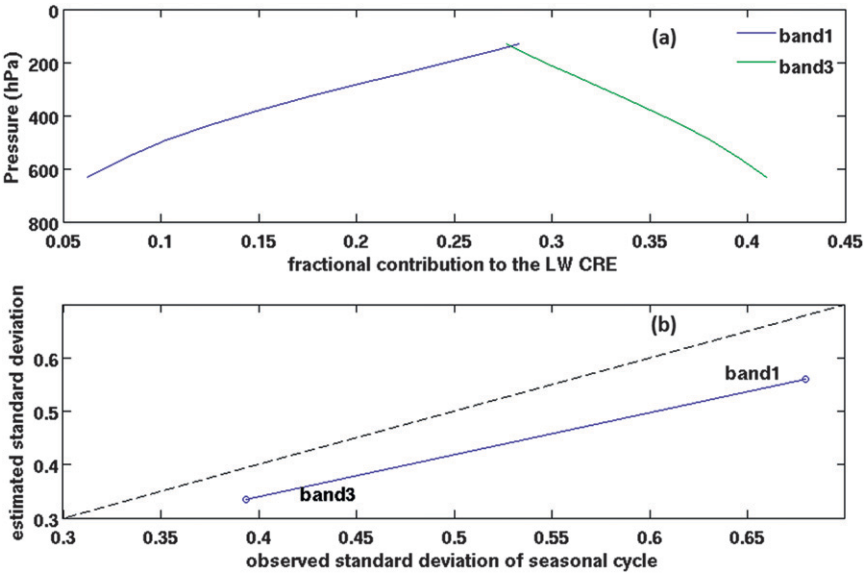

FIG. 7. (a) Change of band 1 f_{CRE} and band 3 f_{CRE} with respect to the cloud-top pressure in a simple conceptual model in which cloud is assumed to be optically thick and typical tropical sounding profiles are used. Radiative calculation is done with MODTRAN5. (b) Observed standard deviations of the seasonal cycles of band 1 f_{CRE} and band 3 f_{CRE} vs estimated counterparts. Black dashed line denotes the 1:1 slope.

These model–observation differences are opposite to those for band 2, for which the GFDL AM2 underestimates over the low-cloud region and the GEOS5 and CanAM4 overestimate over the majority of the tropical oceans. This is another way to expose the compensating biases among different bands in a GCM. As mentioned in section 1 and Huang et al. (2010), such differences in modeled f_{CRE} can be attributed to the differences in cloud-top temperature. The differences between the AM2 and observations over both bands 2 and 3 consistently indicate that, on average, the cloud-top temperature over the low-cloud regions are higher than observed ones, which leads to an overestimation of band 3 f_{CRE} and the underestimation of band 2 f_{CRE}. Similarly, for the GEOS-5, the mean cloud-top temperatures are lower than the observed ones, accounting for the underestimation of band 3 f_{CRE} and the overestimation of band 2 f_{CRE}. Note that it is known that there is still difficulty in simulating temperature profiles in the low-cloud regions (temperature inversion, boundary layer mixing, etc.). So the differences between simulated and observed cloud-top temperature could be due to cloud-top height difference as well as boundary layer temperature difference between models and observations. For the CanAM4, the overestimation for band 2 is generally smaller than in GEOS-5 over the low-cloud regions but still noticeable over certain areas, such as the Peru coast and Namibia coasts, which suggests lower cloud-top temperature than observed ones in these regions.

The observed spatial map of band 4 f_{CRE} (ozone band; Fig. 10e) is similar to that of band 3, owing to the fact that the ozone band is sensitive to the cloud and surface thermal contrast in a similar way as for neighboring bands (i.e., bands 3 and 5). The ozone band in the AM2 model has a bandwidth 30 cm^{-1} shorter than that used in the observations and the GEOS-5 and CanAM4 models (Table 2), which accounts for the consistently smaller contribution in the AM2 (Fig. 10f) than in the observation. GEOS-5 agrees best with observations, even though smaller biases can still be seen over low-cloud regions consistent with those shown in band 3 over the same region. The calculated online ozone profiles continuously updated with the dynamical fields in the GEOS-5 simulation probably contribute to such good agreement. The spatial maps of band 5 f_{CRE} and model-observation difference (not shown here) are similar to those of band 3 because the majority of the radiation of band 5 comes from the second window region (1100–1200 cm^{-1}).

As mentioned in section 2, the GFDL AM2 radiation scheme assumes all clouds to be nonscattering in the LW while the NASA GEOS-5 and CCCma CanAM4 explicitly take the scattering into account (although the treatments are different in GEOS-5 and CanAM4). Therefore, it is meaningful to estimate how much of the difference shown in Figs. 10 and 11 is due to the inclusion of scattering. Similar to Fig. 7, we use the same conceptual model to estimate such difference. In one

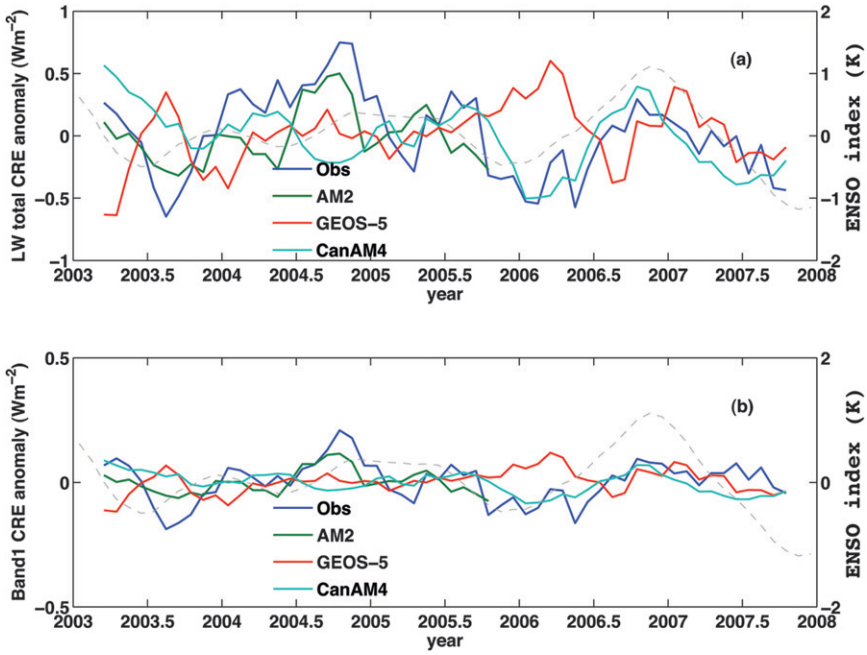

FIG. 8. (a) Five-month running means of deseasonalized anomalies of total LW CRE from the observations (blue line), the GFDL AM2 (green line), NASA GEOS-5 output (red line), and CCCma CanAM4 (cyan line) simulations. The ENSO index is plotted as a gray dashed line. (b) As in (a), but for the band 1 CRE instead of total LW CRE. Following previous studies, the ENSO index is defined as the 5-month running mean of the SST anomalies averaged over the region of 5°S–5°N and the South American coast to 180°W.

case cloud is assumed to be nonscattering and, in another case, the scattering is solved by a four-stream DISORT solver in the MODTRAN5 package (Berk et al. 2005). The f_{CRE} of the nonscattering case is shown in Fig. 12a and the difference between the two cases (scattering − nonscattering) is shown in Fig. 12b. For clouds below 10 km, the difference is negligible except for band 3 and cloud top below 4 km. For clouds above 10 km, there are noticeable differences in all five bands. From 10 to 13 km, the difference is within ±0.03. The

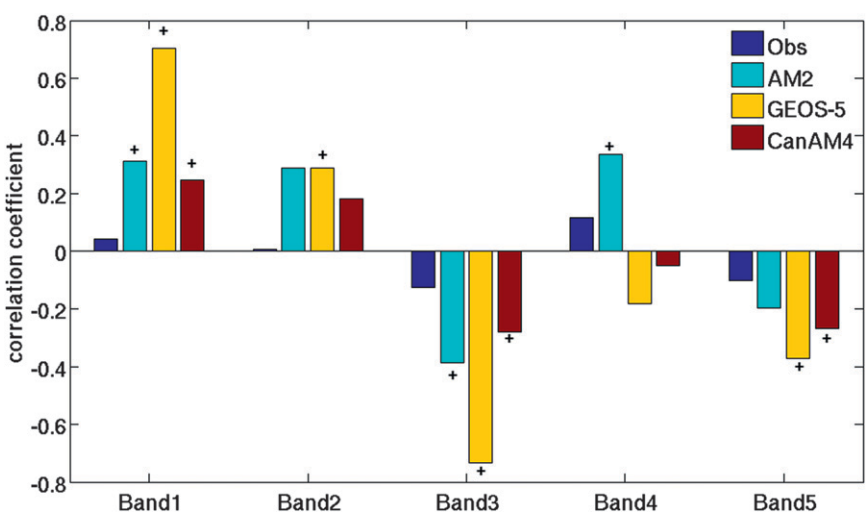

FIG. 9. Correlation coefficients between the ENSO index and the 5-month running means of deseasonalized f_{CRE} of each band. Results from observation and three models are shown in different colors. A plus sign indicates a >90% confidence level.

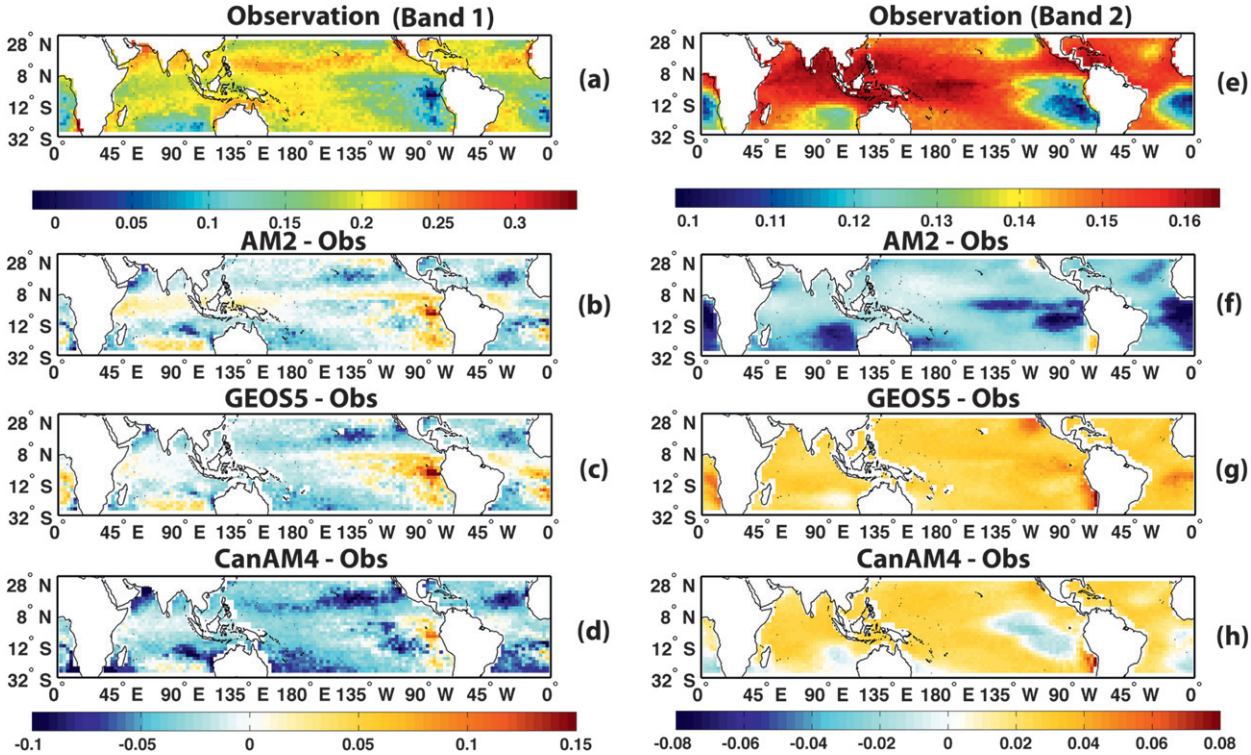

FIG. 10. (a) Map of observed long-term mean of band 1 f_{CRE}. (b)–(d) Maps of model–observation difference in the long-term mean of band 1 f_{CRE} for the GFDL AM2, NASA GEOS-5, and CCCma CanAM4 simulations, respectively. Note the same color scale is used for (b)–(d). (e) As in (a), but for band 2 f_{CRE}. (f)–(h) As in (b)–(d), but for band 2 f_{CRE}.

largest difference (~ -0.09) is seen in band 1 for cloud-top height at 14 km. Such large negative difference can be understood from two aspects: 1) according to Wien's displacement law, for a cloud-top height at 14 km (i.e., cloud-top pressure at ~150 mb and cloud-top temperature around 210 K), the fractional contribution from band 1 is as large as that from band 3 (Fig. 12a); and 2) for ice, the imaginary part of the index of refraction has a minimum value at 410 cm^{-1} (Warren 1984; Warren and Brandt 2008), which means that the inclusion of scattering would lead to the strongest scattering effect around this wavenumber. Overall, Fig. 12b indicates that including scattering in the radiation scheme should have minor or negligible impact on the f_{CRE}, unless the cloud top is very high ($\geq$14 km). Note that over the tropical oceans, only a small fraction clouds can have their tops at or above 14 km (~150 hPa). Cloud profiling radar observations suggest that over the tropical belt this fraction is ~5% or less and is concentrated in the core of the ITCZ (Haynes and Stephens 2007). For the GCMs examined here, the monthly mean cloud fraction above 150 hPa is about the same as the observed. Therefore, the discrepancies between models and observations in either averages or spatial distributions are primarily due to the difference in the modeled and observed cloud properties themselves, and not due to the inclusion of scattering or the details of scattering treatment in the radiation scheme.

b. Composite analysis

In addition to the comparisons of spatial f_{CRE}, we carry out a composite analysis to delineate the dependence of monthly-mean f_{CRE} with respect to the monthly-mean 500-hPa vertical velocity (ω_{500}), an indicator commonly used for the large-scale dynamical regimes (Bony et al. 2004; Bony and Dufresne 2005). For each GCM, its own monthly-mean ω_{500} fields are used accordingly. For observation, the monthly-mean ω_{500} from the interim European Centre for Medium-Range Weather Forecasts (ECMWF) Re-Analysis (ERA-Interim; Dee et al. 2011) are used. The results for bands 1–3 are summarized in Fig. 13. For the large-scale ascending regime ($\omega_{500} < 0$), the composite band 1 and 2 f_{CRE} values gradually decrease as ω_{500} approaches 0. The sharpest change of f_{CRE} is around $\omega_{500} = 0$ for the change from the ascending regime to the subsidence regime. The composited band 1 and band 2 f_{CRE} of three models all level off for strong large-scale subsidence ($\omega_{500} > 0.05$ Pa s^{-1}). The observed band 1 and 2 f_{CRE} composites for such strong subsidence still gradually

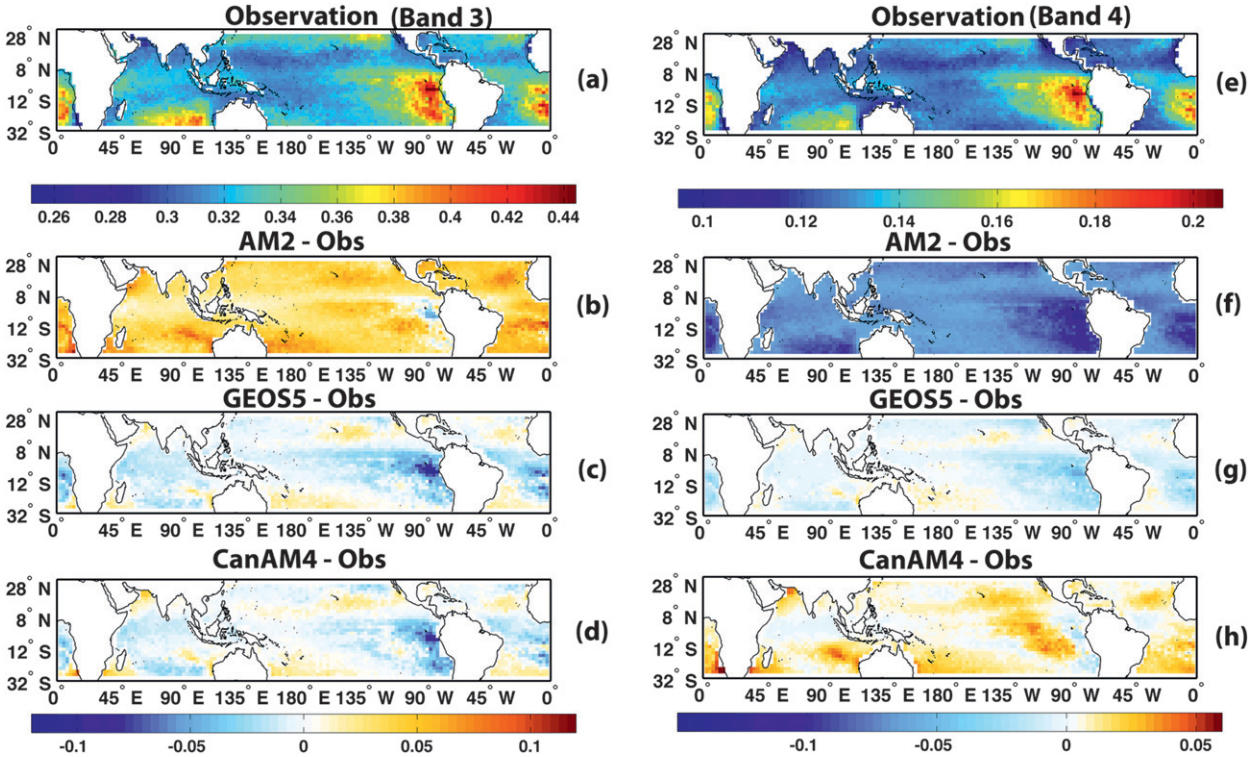

FIG. 11. As in Fig. 10, but for band 3 f_{CRE} and band 4 f_{CRE}.

decrease with the increase of ω_{500}, but statistically they are bracketed within the 1σ deviation from model composite. The behavior of band 3 f_{CRE} is opposite to those of bands 1 and 2 at both the ascending and subsidence regimes. These features are generally consistent with our interpretation of f_{CRE} as a proxy of effective thermal cloud-top height. When ascending becomes weaker, the cloud-top height is expected to be lower so the f_{CRE} of bands 1 and 2 becomes smaller while that of band 3 becomes larger. When subsidence becomes stronger, clouds, if any, are mostly capped within the boundary layer, and therefore f_{CRE} either levels off or changes little with large positive ω_{500}. Consistent with spatial distributions shown in Figs. 10 and 11, the GFDL band 2 f_{CRE} composite is lower than its observed counterpart and its band 3 f_{CRE} composite is higher than its

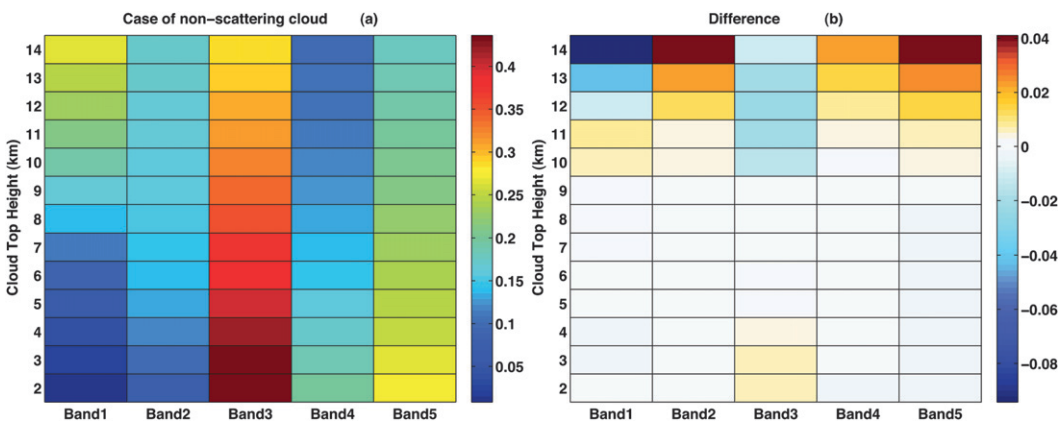

FIG. 12. (a) Band-by-band f_{CRE} for different cloud-top height (2–14 km). Clouds are assumed to be opaque and nonscattering. (b) The difference in f_{CRE} between the case of scattering cloud and the case of nonscattering cloud when everything else remains the same.

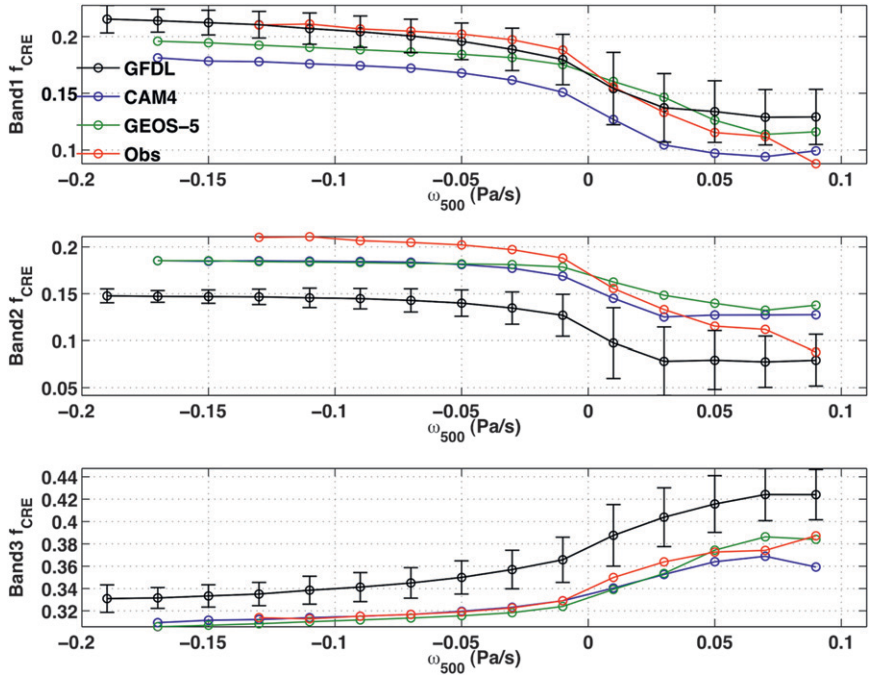

FIG. 13. Composite of the monthly-mean f_{CRE} with respect to the corresponding monthly-mean 500-hPa vertical velocity (ω_{500}). Modeled monthly-mean ω_{500} is used for the (a) band 1, (b) band 2, and (c) band 3 composite. For the observation, ERA-Interim reanalysis of ω_{500} is used. The bin size is 0.02 Pa s^{-1}. For statistical robustness, only bins with more than 0.1% of total data points are calculated here. GFDL, CanAM4, and NASA GEOS-5 results are plotted in black, blue, and green colors, respectively. Observation is plotted in red. The vertical ticks represent the $\pm 1\sigma$ deviation from the composite mean for the GFDL results. The standard deviations of composites of the other two models are similar to that of GFDL.

observed counterpart for all ω_{500} bins. CanAM4 and GEOS-5 composites of band 3 f_{CRE} agree better with observed ones at the ascending branch than at the descending branch, which is also consistent with comparisons of spatial distribution.

5. Conclusions and discussion

Taking advantage of a multiyear multiband LW CRE dataset over the tropical oceans derived from collocated AIRS and CERES observations, this study evaluates in details the LW band-by-band CRE simulated by three different GCMs. It quantitatively demonstrates that, even when the model-simulated broadband LW CRE largely agrees with the observed one, compensating biases from different LW bands can be prominent. The band-by-band CRE differences between models and observations can be as large as the difference in the LW broadband CRE. We prefer to use in our analysis the fractional contribution of each band to the LW CRE, f_{CRE}, which has the unique advantage of being sensitive to cloud-top height–temperature and not sensitive to cloud fraction. This property of f_{CRE} enables us to separate the contribution of cloud fraction and cloud-top height to the top-of-atmosphere LW flux. The averaged f_{CRE} over the tropical oceans, their seasonal cycles, and their interannual variations are documented. Band 1 f_{CRE} (H_2O band) is strongly anticorrelated with band 3 and band 5 f_{CRE} (window regions). The observed seasonal cycle is consistent with the seasonal cycles of ISCCP cloud-top pressure climatology on both the phase and the amplitude. The simulated seasonal cycles of f_{CRE} agree with observations of the phase but not the amplitude, which is much smaller in the simulations, indicating smaller seasonal variations of simulated cloud-top pressure, on average. As for interannual variations, observations and all GCMs agree on the positive (negative) correlations between band 1 f_{CRE} (bands 3 and 5 f_{CRE}) and the ENSO index. Spatial distributions of band-by-band f_{CRE} highlight the large discrepancies between models and observations in the regions with frequent occurrence of low clouds. While the total LW CRE is usually not used for the study of low clouds, fractional CRE contributions are sensitive to the low cloud-top height (or equivalently, low cloud temperature). This complements the diagnostics of low cloud with shortwave

reflectance, which is more sensitive to cloud liquid path than to the cloud-top height–temperature. Cloud-top height only directly affects the shortwave reflectance by changing the amount of solar absorption due to water vapor above the cloud. But the change of cloud-top height dominates the change of LW band-by-band f_{CRE}. Therefore, such band-by-band f_{CRE} offers a useful diagnostics for the low clouds simulated by the models.

While this analysis focuses on f_{CRE} for the reason articulated in section 1, both the absolute LW CRE and f_{CRE} of each band are important to diagnose the quality of cloud simulations. Cloud fraction significantly affects the absolute LW CRE while f_{CRE} is more sensitive to cloud-top height/temperature. If a model is poor in producing correct cloud fractions for a certain type of cloud (e.g., the underestimation of low cloud fractions in the GEOS-5 model as noted in comparison with observed low cloud fractions), it would be logical and practical to first address the issue of cloud fraction and then evaluate the f_{CRE}. For both model evaluation and cloud feedback study, f_{CRE} is a meaningful metric to use and it complements the absolute broadband LW CRE.

Recently considerable effort has been invested to develop satellite simulators that reconcile cloud field views from the satellite and model perspectives, for example, the ISCCP simulator by Klein and Jakob (1999) and the recent COSP simulator (Bodas-Salcedo et al. 2011) adopted by many modeling centers. The objective of such simulator is to ensure fair comparisons between simulated and retrieved cloud variables, such as cloud-top height (CTH), cloud-top pressure (CTP), or cloud-top temperature (CTT). We think that the information content of f_{CRE} diagnostics does not overlap with that of cloud-related satellite simulator diagnostics, but is rather complimentary and enhances our understanding of simulated clouds. Here is why:

1) Except for specialized case studies with additional coding efforts, essentially all GCM evaluations or data–model comparisons involve spatial or temporal averages or both (e.g., the commonly used monthly-mean datasets). While relations between TOA radiative quantities (flux and CRE) and geophysical parameters at any given moment are relatively easy to understand, the relations between averaged TOA quantities and averaged geophysical parameters sometimes are much more difficult to interpret. This is because of the strong nonlinearity between the TOA radiative quantities and geophysical parameters (e.g., the dependence of OLR on cloud-top height) as well as the way that averaging is performed. For example, a simple arithmetic monthly average of CTP is not equivalent to a simple arithmetic monthly average of CTH. The value of $f_{CRE,}$ on the other hand, is intrinsically related to TOA LW CRE and the radiation budget.
2) For passive remote sensing products such as ISCCP and MODIS, CTH, CTP, and CTT are secondary estimated values in retrieval process. For monthly averages of such quantities (the level-3 product), they are strongly influenced by cloud detection techniques. Moreover, large discrepancies could exist among satellite products due to different techniques used in cloud-top height estimation (e.g., CO_2 slicing method vs 11-μm radiance estimation). For example, Garay et al. (2008) showed that, over the southeastern Pacific, ISCCP CTH retrievals were found to be biased high by 1.4–2 km while MODIS was biased high by more than 2 km. Furthermore, the differences between simulated and observed vertical temperature profiles further complicate any comparisons between satellite-observed and modeled CTP and CTT.

Therefore, f_{CRE} provides useful diagnostics of the vertical location of simulated cloud fields and complements nicely diagnostics based on the satellite–simulator approach. To completely understand the connections among model biases in LW radiation budget and CRE, in f_{CRE}, in cloud fields as seen in a satellite simulator, and in temperature and humidity fields is beyond the scope of this study but is a focal point of our ongoing follow-up studies.

To our knowledge, this is the first study to compare the simulated band-by-band LW CRE from multiple GCMs. While the results of the ozone bands are difficult to interpret, largely because of inconsistent treatments of the ozone in the model, they do show that different treatment of ozone affects not only the chemistry but also the LW CRE and radiation budget at such a band-by-band level. The good agreement between NASA GEOS-5 and observation in the ozone band CRE (Fig. 11) suggests that, when the detailed band-by-band decompositions of LW CRE are scrutinized against observations, the effect of ozone cannot be neglected. This has implications for the tuning of GCMs to match the TOA energy balance as well as the climate projections in the presence of ozone recovery. Generally speaking, it is possible, if not very likely, to tune GCM to achieve a the TOA balance between outgoing longwave flux and net incoming shortwave flux for current climate while the band-by-band decomposition of LW flux (or LW CRE) is different from that observed. For example, the bias in the TOA energy imbalance due to simple representation of time-varying ozone fields can be ''tuned'' away by adjusting some less-constrained parameters in various

GCM parameterization schemes. What is unknown, however, is what the consequences would be for future climate projection simulated by the same GCM when such incorrect band-by-band composition of TOA flux for the current climate exists. Our future work will try to address this kind of question by analyzing the band-by-band flux and CRE from simulations carried out for different future scenarios prescribed by the Intergovernmental Panel on Climate Change (IPCC) assessment.

Acknowledgments. We wish to thank H.W. Chuang for her assistance in data processing at the early stage of this work. We also thank two reviewers for their thorough and thoughtful comments. The lead author is greatly indebted to NOAA GFDL for the generosity of providing computing resources for the GFDL AM2 simulation. The AIRS data were obtained from NASA GSFC DAAC and the CERES data from NASA Langley DAAC. This research is supported by NSF AGS CLD program under Grant NSF ATM 0755310 and NASA *Terra*/*Aqua* program under Grant NNX11AH55G awarded to the University of Michigan. L. Oreopoulos acknowledges funding support from NASA's Modeling Analysis and Prediction program managed by Dr. D. Considine.

REFERENCES

Allan, R. P., and M. A. Ringer, 2003: Inconsistencies between satellite estimates of longwave cloud forcing and dynamical fields from reanalyses. *Geophys. Res. Lett.,* **30,** 1491, doi:10.1029/2003GL017019.

——, ——, J. A. Pamment, and A. Slingo, 2004: Simulation of the Earth's radiation budget by the European Centre for Medium-Range Weather Forecasts 40-year reanalysis (ERA40). *J. Geophys. Res.,* **109,** D18107, doi:10.1029/2004JD004816.

Anderson, J. L., and Coauthors, 2004: The new GFDL global atmosphere and land model AM2–LM2: Evaluation with prescribed SST simulations. *J. Climate,* **17,** 4641–4673.

Berk, A., and Coauthors, 2005: MODTRAN5: A reformulated atmospheric band model with auxiliary species and practical multiple scattering options. *Multispectral and Hyperspectral Remote Sensing Instruments and Applications II,* A. M. Larar, M. Suzuki, and Q. Tong, Eds., International Society for Optical Engineering (SPIE Proceedings, Vol. 5655), doi:10.1117/12.578758.

Bodas-Salcedo, A., and Coauthors, 2011: COSP: Satellite simulation software for model assessment. *Bull. Amer. Meteor. Soc.,* **92,** 1023–1043.

Bony, S., and J. L. Dufresne, 2005: Marine boundary layer clouds at the heart of tropical cloud feedback uncertainties in climate models. *Geophys. Res. Lett.,* **32,** L20806, doi:10.1029/2005GL023851.

——, ——, H. Le Treut, J.-J. Morcrette, and C. Senior, 2004: On dynamic and thermodynamic components of cloud changes. *Climate Dyn.,* **22,** 71–86.

Chou, M.-D., M. J. Suarez, X.-Z. Liang, and M. M.-H. Yan, 2003: A thermal infrared radiation parameterization for atmospheric studies. NASA Technical Report Series on Global Modeling and Data Assimilation, NASA/TM-2001-104606, Vol. 19, 65 pp. [Available online at http://ntrs.nasa.gov/archive/nasa/casi.ntrs.nasa.gov/20010072848_2001122986.pdf.]

Cionni, I., and Coauthors, 2011: Ozone database in support of CMIP5 simulations: Results and corresponding radiative forcing. *Atmos. Chem. Phys.,* **11,** 11 267–11 292, doi:10.5194/acp-11-11267-2011.

Dee, D. P., and Coauthors, 2011: The ERA-Interim reanalysis: Configuration and performance of the data assimilation system. *Quart. J. Roy. Meteor. Soc.,* **137,** 553–597.

Deser, C., and J. M. Wallace, 1990: Large-scale atmospheric circulation features of warm and cold episodes in the tropical Pacific. *J. Climate,* **3,** 1254–1281.

Fu, R., W. T. Liu, and R. E. Dickinson, 1996: Response of tropical clouds to the interannual variation of sea surface temperature. *J. Climate,* **9,** 616–634.

Garay, M. J., S. P. de Szoeke, and C. M. Moroney, 2008: Comparison of marine stratocumulus cloud top heights in the southeastern Pacific retrieved from satellites with coincident ship-based observations. *J. Geophys. Res.,* **113,** D18204, doi:10.1029/2008JD009975.

Haynes, J. M., and G. L. Stephens, 2007: Tropical oceanic cloudiness and the incidence of precipitation: Early results from CloudSat. *Geophys. Res. Lett.,* **34,** L09811, doi:10.1029/2007GL029335.

Huang, X., V. Ramaswamy, and M. D. Schwarzkopf, 2006: Quantification of the source of errors in AM2 simulated tropical clear-sky outgoing longwave radiation. *J. Geophys. Res.,* **111,** D14107, doi:10.1029/2005JD006576.

——, W. Z. Yang, N. G. Loeb, and V. Ramasawamy, 2008: Spectrally resolved fluxes derived from collocated AIRS and CERES measurements and their application in model evaluation: Clear sky over the tropical oceans. *J. Geophys. Res.,* **113,** D09110, doi:10.1029/2007JD009219.

——, N. G. Loeb, and W. Z. Yang, 2010: Spectrally resolved fluxes derived from collocated AIRS and CERES measurements and their application in model evaluation: 2. Cloudy sky and band-by-band cloud radiative forcing over the tropical oceans. *J. Geophys. Res.,* **115,** D21101, doi:10.1029/2010JD013932.

Huang, Y., V. Ramaswamy, X. Huang, Q. Fu, and C. Bardeen, 2007: A strict test in climate modeling with spectrally revolved radiances: GCM simulation versus AIRS observations. *Geophys. Res. Lett.,* **34,** L24707, doi:10.1029/2007GL031409.

Klein, S. A., and C. Jakob, 1999: Validation and sensitivities of frontal clouds simulated by the ECMWF model. *Mon. Wea. Rev.,* **127,** 2514–2531.

——, B. J. Soden, and N.-C. Lau, 1999: Remote sea surface temperature variations during ENSO: Evidence for a tropical atmospheric bridge. *J. Climate,* **12,** 917–932.

Li, J., 2002: Accounting for unresolved clouds in a 1D infrared radiative transfer model. Part I: Solution for radiative transfer, including cloud scattering and overlap. *J. Atmos. Sci.,* **59,** 3302–3320.

——, and Q. Fu, 2000: Absorption approximation with scattering effect for infrared radiation. *J. Atmos. Sci.,* **57,** 2905–2914.

——, and H. W. Barker, 2005: A radiation algorithm with correlated-*k* distribution. Part I: Local thermal equilibrium. *J. Atmos. Sci.,* **62,** 286–309.

McClatchey, R. A., R. W. Fenn, J. E. A. Selby, J. S. Garing, and F. E. Volz, 1972: Optical properties of the atmosphere. 3rd ed. Air Force Cambridge Research Laboratories Tech. Rep. AFCRL-72-0497, 80 pp.

Molod, A., L. Takacs, M. Suarez, J. Bacmeister, I.-S. Song, and A. Eichmann, 2012: The GEOS-5 atmospheric general

circulation model: Mean climate and development from MERRA to Fortuna. NASA Technical Report Series on Global Modeling and Data Assimilation, NASA/TM-2008-104606, Vol. 28, 112 pp. [Available online at http://ntrs.nasa.gov/archive/nasa/casi.ntrs.nasa.gov/20120011790_2012011404.pdf.]

Paul, J., F. Fortuin, and H. Kelder, 1998: An ozone climatology based on ozonesonde and satellite measurements. *J. Geophys. Res.,* **103** (D24), 31 709–31 734.

Pincus, R., H. W. Barker, and J.-J. Morcrette, 2003: A fast, flexible, approximate technique for computing radiative transfer in inhomogeneous cloud fields. *J. Geophys. Res.,* **108,** 4376, doi:10.1029/2002JD003322.

Ramanathan, V., R. D. Cess, E. F. Harrison, P. Minnis, B. R. Barkstrom, E. Ahmad, and D. Hartmann, 1989: Cloud-radiative forcing and climate: Results from the Earth Radiation Budget Experiment. *Science,* **243,** 57–63.

Raval, A., A. H. Oort, and V. Ramaswamy, 1994: Observed dependence of outgoing longwave radiation on sea surface temperature and moisture. *J. Climate,* **7,** 807–821.

Rienecker, M. M., and Coauthors, 2008: The GEOS-5 Data Assimilation System—Documentation of versions 5.0.1, 5.1.0, and 5.2.0. NASA Technical Report Series on Global Modeling and Data Assimilation, NASA/TM-2008-104606, Vol. 27, 118 pp.

Rossow, W. B., and R. A. Schiffer, 1991: ISCCP cloud data products. *Bull. Amer. Meteor. Soc.,* **72,** 2–20.

——, and ——, 1999: Advances in understanding clouds from ISCCP. *Bull. Amer. Meteor. Soc.,* **80,** 2261–2288.

Schwarzkopf, M. D., and V. Ramaswamy, 1999: Radiative effects of CH_4, N_2O, halocarbons and the foreign-broadened H_2O continuum: A GCM experiment. *J. Geophys. Res.,* **104** (D8), 9467–9488.

Slingo, A., J. A. Pamment, and M. J. Webb, 1998: A 15-year simulation of the clear-sky greenhouse effect using the ECMWF reanalyses: Fluxes and comparisons with ERBE. *J. Climate,* **11,** 690–708.

Warren, S. G., 1984: Optical constants of ice from the ultraviolet to the microwave. *Appl. Opt.,* **23,** 1206–1225.

——, and R. E. Brandt, 2008: Optical constants of ice from the ultraviolet to the microwave: A revised compilation. *J. Geophys. Res.,* **113,** D14220, doi:10.1029/2007JD009744.

Wielicki, B. A., and Coauthors, 2002: Evidence for large decadal variability in the tropical mean radiative energy budget. *Science,* **295,** 841–844.

Wong, T., B. A. Wielicki, R. B. Lee, G. L. Smith, K. A. Bush, and J. K. Willis, 2006: Reexamination of the observed decadal variability of the earth radiation budget using altitude-corrected ERBE/ERBS nonscanner WFOV data. *J. Climate,* **19,** 4028–4040.

Yang, S.-K., Y.-T. Hou, A. J. Miller, and K. A. Campana, 1999: Evaluation of the earth radiation budget in NCEP–NCAR reanalysis with ERBE. *J. Climate,* **12,** 477–493.